FRONTIERS OF PHYSICS

RESEARCH ARTICLE
Volume 19 / Issue 4 / 43204 / 2024

High performance photodetector based on few-layer $MoTe_2/CdS_{0.42}Se_{0.58}$ flake heterojunction

Ran Ma[1], Qiuhong Tan[1,2,3,†], Peizhi Yang[3], Yingkai Liu[1,2,3], Qianjin Wang[1,2,3,‡]

1 College of Physics and Electronic Information, Yunnan Normal University, Kunming 650500, China
2 Yunnan Provincial Key Laboratory for Photoelectric Information Technology, Yunnan Normal University, Kunming 650500, China
3 Key Laboratory of Advanced Technique & Preparation for Renewable Energy Materials, Ministry of Education, Yunnan Normal University, Kunming 650500, China
Corresponding authors. E-mail: †tanqiuhong1@126.com, ‡qjwang@xtu.edu.cn
Received October 5, 2023; accepted December 3, 2023

ABSTRACT

Two-dimensional (2D) transition metal dichalcogenides have been extensively studied due to their fascinating physical properties for constructing high-performance photodetectors. However, their relatively low responsivities, current on/off ratios and response speeds have hindered their widespread application. Herein, we fabricated a high-performance photodetector based on few-layer $MoTe_2$ and $CdS_{0.42}Se_{0.58}$ flake heterojunctions. The photodetector exhibited a high responsivity of 7221 A/W, a large current on/off ratio of 1.73×10^4, a fast response speed of 90/120 μs, external quantum efficiency (EQE) reaching up to 1.52×10^6 % and detectivity (D^*) reaching up to 1.67×10^{15} Jones. The excellent performance of the heterojunction photodetector was analyzed by a photocurrent mapping test and first-principle calculations. Notably, the visible light imaging function was successfully attained on the $MoTe_2/CdS_{0.42}Se_{0.58}$ photodetectors, indicating that the device had practical imaging application prospects. Our findings provide a reference for the design of ultrahigh-performance $MoTe_2$-based photodetectors.

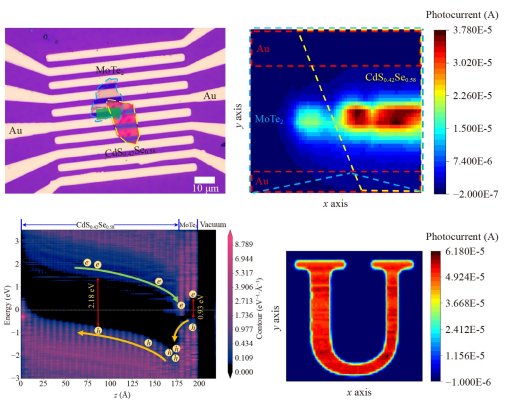

Keywords photodetector, $MoTe_2$, heterojunction, visible light imaging, first-principles calculations

1 Introduction

2D layered materials have facilitated a new era in fundamental research and exploration of their potential applications [1]. Numerous 2D layered materials, including graphene, hexagonal boron nitride, black phosphorus, transition metal dichalcogenides (TMDs), and post-transition metal dichalcogenides, have garnered significant attention due to their exceptional structures and intriguing physical and chemical properties [2–6]. Importantly, 2D materials have potential applications in a wide range of research fields, such as catalysis [7–11], batteries [12–16], phototransistors [17–21], and photodetectors [22–26].

As a member of TMDs, $MoTe_2$ is a layer-dependent band gap (1.0–1.1 eV) semiconductor and is an attractive candidate for high-performance photodetectors because of its stability and outstanding electrical and optical performances; for example, $MoTe_2$ has strong light absorption and high carrier mobility. However, the single $MoTe_2$ photodetector exhibits a relatively low

#Special Topic: Two-dimensional Electronic Materials and Devices (Eds.: Lin Wang & Xiaolong Chen).

Higher Education Press

https://doi.org/10.1007/s11467-023-1374-3

ratio of photocurrent to dark current, response speed (millisecond level) and low responsivity (mA/W level) [27]; these aspects hinder its further application in light detection. Based on this situation, many researchers have carried out numerous studies to improve the photoelectric performance by applying a gate voltage or constructing heterostructures. Wright *et al.* [28] fabricated four-layer $MoTe_2$ field effect transistors (FETs) with a photoresponse time of ~160 μs under 685 nm laser illumination, and the photoresponsivity was only 6 A/W even when a large gate voltage of –40 V was applied. He *et al.* [29] also reported a $MoTe_2$ phototransistor, which exhibited a responsivity of ~10^2 A/W at zero gate voltage with an increase reaching up to 2560 A/W at 80 V gate voltage under 473 nm laser illumination. Chu *et al.* [30] developed a few-layer $MoTe_2$ photodetector, which demonstrated a photoresponsivity of 50 mA/W and a detectivity of 3.1 × 10^9 cm·$Hz^{1/2}$·W^{-1} for 637 nm light at a back gate voltage of 10 V. Then, they designed a self-powered $MoTe_2/MoS_2$ vertical heterojunction photodetector, which possessed a high on/off ratio (>10^5) and a fast response time of 60 μs. However, the photoresponsivity remained relatively low at 46 mA/W [31]. Lu *et al.* [32] fabricated a 1D Ga-doped CdS nanowire/2D $MoTe_2$ flake heterojunction device, achieving a self-driven photodetector with a response time of less than 50 ms and a photoresponsivity of less than 60 mA/W. Chen *et al.* [33] fabricated a $MoTe_2/WSe_2$ heterojunction photodetector, achieving a high on/off ratio of ~10^4 and a low response time of 72 μs under illumination with a 633 nm laser; however, the responsivity was only 1.8 mA/W. Jie *et al.* [34] reported a few-layer $MoTe_2$/Si 2D–3D vertical heterojunction photodetector. Their device possessed an ultrahigh response speed up to 150 ns and a large on/off ratio of 3.2 × 10^6 under 980 nm light illumination; however, the responsivity and the EQE were only 0.19 A/W and 24%, respectively. Although much work has been carried out in $MoTe_2$-based photodetectors, some key parameters (such as responsivity) still need significant improvement. Moreover, numerous research has been performed on visible light imaging of $MoTe_2$-based photodetectors. Therefore, more efforts need to be made to improve the photodetection performance of the $MoTe_2$-based photodetectors. Constructing heterojunctions is considered an effective method to improve the photoelectric performance of photodetectors via energy band engineering; this engineering can enhance the photocurrent, suppress the dark current and promote the effective separation of the photogenerated carriers. Loutfy *et al.* [35] reported that $CdS_{0.5}Se_{0.5}$ had the highest photoelectrochemical conversion efficiency, achieved by optimizing the composition in $CdS_{1-x}Se_x$ thin films. Additionally, we successfully fabricated high-quality $CdS_{0.42}Se_{0.58}$ flakes, in which the composition was similar to that of $CdS_{0.5}Se_{0.5}$. To the best of our knowledge, few-layer $MoTe_2$ and $CdS_{0.42}Se_{0.58}$ flake heterojunctions have not yet been reported.

In this work, we fabricated a $MoTe_2/CdS_{0.42}Se_{0.58}$ flake heterojunction to achieve a high-performance photodetector, with high responsivity (7221 A/W), large current on/off ratio (1.73 × 10^4), fast response speed (90/120 μs), large EQE (1.52 × 10^6 %) and detectivity (1.67 × 10^{15} Jones). In view of the high performance, we investigated the visible light imaging of heterojunction devices, which indicated the great potential of $MoTe_2/CdS_{0.42}Se_{0.58}$ photodetectors for room-temperature visible imaging. The microphysical mechanism of the excellent performance of the $MoTe_2/CdS_{0.42}Se_{0.58}$ photodetectors was determined based on DFT calculations. Our study has shown that the $MoTe_2/CdS_{0.42}Se_{0.58}$ heterojunction has potential applications in high-performance photodetectors due to its excellent optical properties and imaging capabilities.

2 Experimental section

2.1 Preparation of $CdS_{0.42}Se_{0.58}$ and $MoTe_2$ flakes

The $CdS_{0.42}Se_{0.58}$ material was synthesized within a tubular furnace outfitted with a quartz tube measuring 25 mm in diameter. Initially, high-purity CdS and CdSe powders with a purity of 99.99% were combined in a ceramic boat in a 1:1 molar ratio. Subsequently, the mixture was placed in the central evaporation zone within the quartz tube. Next, silicon wafers were cut into slices measuring 1.5 cm × 1.0 cm and immersed in a beaker containing acetone. After undergoing ultrasonic cleaning for 10 minutes in the acetone solution, the silicon substrates were further rinsed for 10 minutes with deionized water. Following the cleaning process, the silicon substrates were coated with a layer of gold particles and positioned at the upstream and downstream ends of the quartz tube. Finally, the quartz tube was introduced into the tubular furnace, and the temperature was gradually increased to 835 °C at a rate of 5.6 °C/min. The system was maintained at this temperature for 150 minutes under a flow of 17 sccm Ar:H_2 gas mixture with a ratio of 95:5. Subsequently, the furnace was allowed to naturally cool to room temperature, and the $CdS_{0.42}Se_{0.58}$ flake was obtained. The few-layer $MoTe_2$ flake was obtained by a mechanical exfoliation method.

2.2 Preparation of the $MoTe_2/CdS_{0.42}Se_{0.58}$ heterojunction photodetector

First, Cr and Au were sequentially deposited on a clean silicon substrate by using electron beam evaporation equipment to form electrodes with a channel length of 5 μm. Second, the $MoTe_2$ flake was transferred to the gold electrodes by a 2D material transfer system. Subsequently, the fabricated $CdS_{0.42}Se_{0.58}$ flakes were soaked

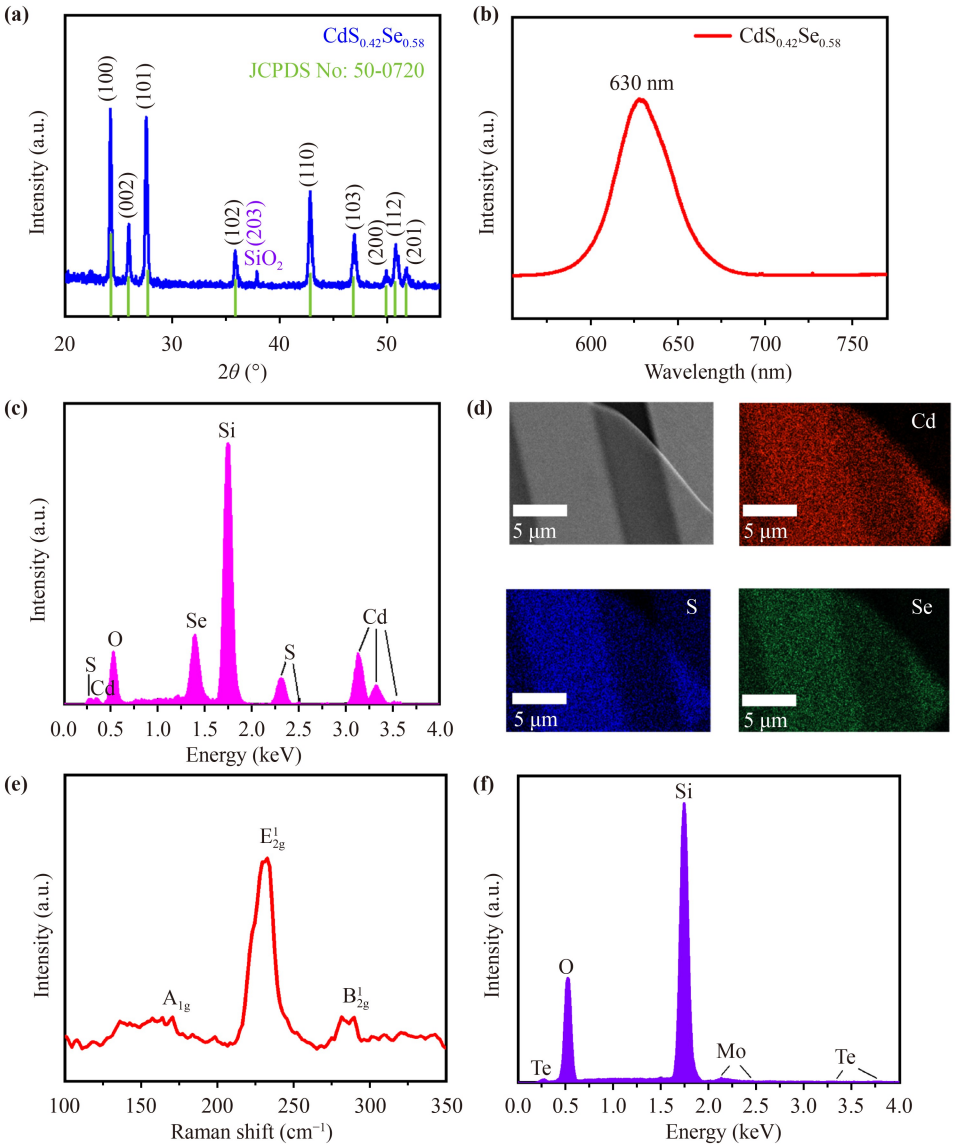

Fig. 1 **(a)** XRD pattern, **(b)** PL, **(c)** EDS and **(d)** elemental mapping of $CdS_{0.42}Se_{0.58}$ flake. **(e)** Raman spectroscopy and **(f)** EDS of few-layer $MoTe_2$ flake.

in an ethanol solution and then added dropwise onto another clean silicon substrate. The $CdS_{0.42}Se_{0.58}$ flake remained on the substrate following the evaporation of ethanol. Finally, the $CdS_{0.42}Se_{0.58}$ flake was detached from the initial substrate and placed above the $MoTe_2$ flake using a PDMS film, thus completing the construction of the heterojunction device.

2.3 First-principles calculations

All first-principles calculations were performed within the framework of the DFT-LCAO method as implemented in the QuantumATK T-2022.03-SP1 software package [36]. To simulate the trilayer $MoTe_2/CdS_{0.42}Se_{0.58}$ heterojunction, a slab model consisting of 336 atoms was built. The vacuum layer thickness was ~22 Å, and the atomic ratios of Cd, S and Se agreed with the experimental values of 1:0.42:0.58 in $CdS_{0.42}Se_{0.58}$ NB. The Grimme DFT-D2 method [37] was adopted in the structure optimization to consider the van der Waals correction. The total energy and force converged to ~10^{-4} eV and 0.05 eV/Å, respectively. The cutoff energy and k-point grid were set to 105 Hartrees and 4 × 4 × 1, respectively. The HSE hybrid functional was used to more accurately calculate the projected density of states of the heterostructure.

3 Results and discussion

Figure 1(a) shows the X-ray diffraction (XRD) pattern of the $CdS_{0.42}Se_{0.58}$ flake. Evidently, the diffraction peak

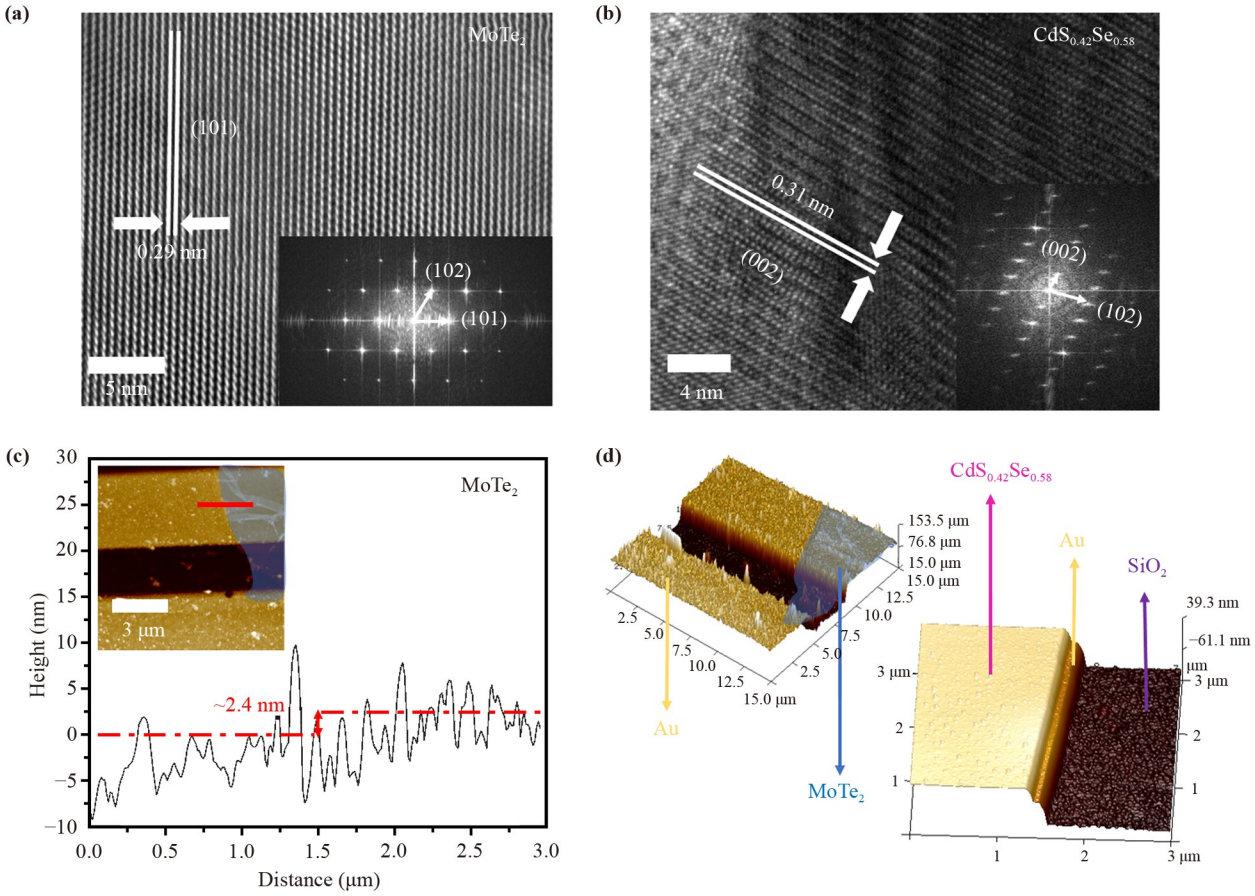

Fig. 2 HRTEM images of **(a)** $MoTe_2$ and **(b)** $CdS_{0.42}Se_{0.58}$. Insets are the corresponding FFT patterns. **(c)** AFM profile along the red line in the inset. The inset is the 2D AFM of the isolated $MoTe_2$ region in the heterojunction device. **(d)** 3D AFM topographies of isolated $MoTe_2$ and $CdS_{0.42}Se_{0.58}$ regions in the heterojunction device.

is consistent with the JCPDS No: 50-0720 standard card [38], in which the ratio of S to Se is 0.42:0.58. A small peak emerged at approximately $2\theta = 37.8°$, which correlates to the (203) diffraction peak of the SiO_2 substrate by comparison with the JCPDS No: 47-1300 card. Figure 1(b) shows the photoluminescence (PL) spectra for the $CdS_{0.42}Se_{0.58}$ flake. A peak is observed at a wavelength of 630 nm; from this peak, the band gap of $CdS_{0.42}Se_{0.58}$ is calculated to be approximately 1.9 eV. Figure 1(c) shows the energy-dispersive X-ray spectroscopy (EDS) of the $CdS_{0.42}Se_{0.58}$ flake. Si, O, Cd, Se, and S are present in the $CdS_{0.42}Se_{0.58}$ flake, in which Si and O originate from the SiO_2 substrate. Figure 1(d) shows the elemental mapping image of the $CdS_{0.42}Se_{0.58}$ flake. These elements are evenly distributed in the $CdS_{0.42}Se_{0.58}$ flake. The magnified SEM showed exceptionally smooth surfaces of the $CdS_{0.42}Se_{0.58}$ flake, demonstrating the excellent crystalline quality of the $CdS_{0.42}Se_{0.58}$ flakes. Figure 1(e) shows the Raman spectrum of the few-layer $MoTe_2$ flake; the layer number of $MoTe_2$ obtained by mechanical exfoliation is 3 layers according to the positions and intensities of the A_{1g}, E^1_{2g} and B^1_{2g} vibration modes in the Raman spectrum [32]. Figure 1(f) shows the EDS diagram of the few-layer $MoTe_2$ flake. The EDS diagram clearly shows the presence of Mo, Te, O, and Si, providing conclusive evidence that the few-layer $MoTe_2$ flake consists of Mo and Te, while elements O and Si can be attributed to the SiO_2 substrate. The relatively low detected values of Te and Mo can be attributed to the thin $MoTe_2$ layer and the abundant distribution of the SiO_2 substrate.

To further investigate the morphology, crystal structure, and surface roughness of the fabricated $MoTe_2$ and $CdS_{0.42}Se_{0.58}$ flakes, we carried out high-resolution transmission electron microscopy (HRTEM) and atomic force microscopy (AFM) measurements. Figures 2(a) and (b) show the HRTEM images of the $MoTe_2$ and $CdS_{0.42}Se_{0.58}$ flakes, respectively; the lattice spacings of 0.29 and 0.31 nm corresponded to the (101) and (002) planes of $MoTe_2$ and $CdS_{0.42}Se_{0.58}$, respectively. The fast Fourier transform (FFT) images (insets) of the two materials indicated their high-quality single-crystalline nanostructure. The step height of 2.4 nm at the edge of the flake indicated that the exfoliated $MoTe_2$ flake was trilayer [see Fig. 2(c)]; this result effectively agreed with the Raman spectral analysis. The 3D AFM topographies [see

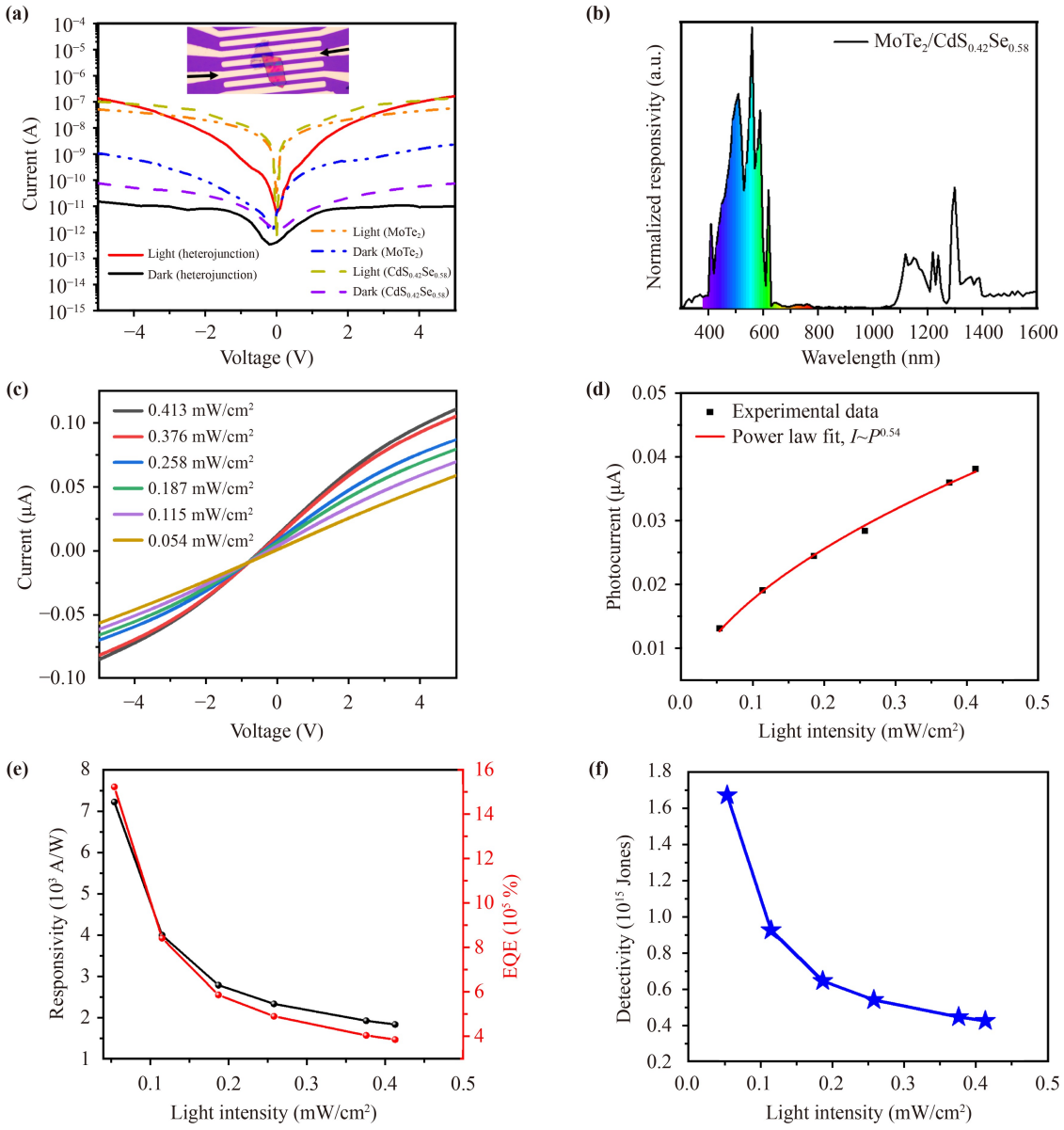

Fig. 3 **(a)** I–V curves of the single few-layer $MoTe_2$ flake, single $CdS_{0.42}Se_{0.58}$ flake and $MoTe_2/CdS_{0.42}Se_{0.58}$ flake heterojunction devices under white light of 1.5 mW/cm^2. The inset is an optical image of the device, in which the black arrows point to the selected test electrodes. **(b)** Responsivity as a function of the illumination wavelength. **(c)** I–V curves of the device with different light power densities. **(d)** Photocurrent as a function of light intensity. **(e)** Dependence of R, EQE and **(f)** D^* with respect to power density under 560 nm light irradiation at a 5 V bias.

Fig. 2(d)] indicated a smooth surface of the fabricated $MoTe_2$ and $CdS_{0.42}Se_{0.58}$ flakes.

Figure 3(a) plots the current–voltage (I–V) curve of the few-layer $MoTe_2/CdS_{0.42}Se_{0.58}$ flake heterojunction photodetector under dark and white-light illumination. For comparison, the I–V characteristics of the single $MoTe_2$ and $CdS_{0.42}Se_{0.58}$ devices were also plotted under the same conditions. The photocurrent drastically increased with increasing bias voltage. At a bias of 5 V, the $MoTe_2$ device showed a low on/off current ratio (~24) due to its high dark current. For the $CdS_{0.42}Se_{0.58}$ device, the on/off current ratio reached up to 1.87×10^3 because of its high photocurrent and low dark current. When the two materials were coupled to form a heterojunction, the photocurrent slightly increased (1.66×10^{-7} A), while the dark current decreased by almost one order of magnitude (9.62×10^{-12} A) compared to that of the $CdS_{0.42}Se_{0.58}$ device. This significant dark current suppression resulted in the on/off current ratio of the device reaching a high value of 1.73×10^4. Therefore, the $MoTe_2/CdS_{0.42}Se_{0.58}$ flake heterojunction photodetector exhibited enhanced photoelectric performance. Figure 3(b) shows the spectral response of the heterojunction photodetector ranging from 300 to 1600 nm.

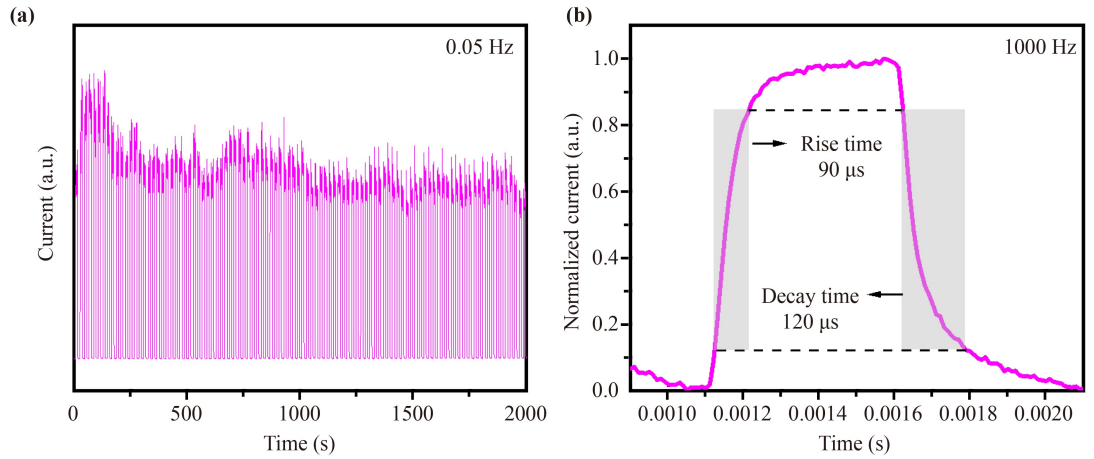

Fig. 4 **(a)** Long-cycle stability measurement of the few-layer $MoTe_2/CdS_{0.42}Se_{0.58}$ heterojunction photodetector. **(b)** Response speeds under a switching frequency of 1 kHz.

Evidently, the heterojunction device showed a strong response to visible (400–600 nm) and near-infrared (1100–1400 nm) wavelengths, corresponding to the bandgap of $CdS_{0.42}Se_{0.58}$ and $MoTe_2$, respectively. These results indicated that excitons in both blocks contributed to the photocurrent. Figure 3(c) shows the *I*–*V* curves of the few-layer $MoTe_2/CdS_{0.42}Se_{0.58}$ flake heterojunction photodetector under different light intensities at 560 nm light illumination. Clearly, the photocurrent increased with increasing light power density at the same bias voltage, indicating that the number of photogenerated carriers was proportional to the absorbed photon flux. When the light power density was 0.413 mW/cm^2, the photocurrent reached 1.11 × 10^{-7} A at 5 V bias, and the switching ratio of the device was calculated to be 1.15 × 10^4 under monochromatic light. Compared with white light illumination, the on/off ratio was reduced but still remained on the same order of magnitude. Figure 3(d) shows the relationship between the photocurrent and light intensity of the few-layer $MoTe_2/CdS_{0.42}Se_{0.58}$ photodetector at a bias of 1 V. The power law formula is as follows: $I_p = AP^{\alpha}$ [39], where I_p is the photocurrent, A is the proportional coefficient, P is the light power density, and exponent α is the fitting coefficient and reflects the trapping and recombination activity of photocarriers. The α value was determined to be 0.54 using the above fitting formula; this result indicated the existence of trap states in the contact interface, which affected the capture and recombination of photogenerated carriers [40].

To further investigate the performance of the few-layer $MoTe_2/CdS_{0.42}Se_{0.58}$ flake heterojunction photodetector, some key parameters of the photodetector were calculated. As is well known, R [41], EQE [42] and D^* [43] are three important parameters for the study of the photoelectric performance of the device, and these parameters can be calculated using the following formulae:

$$R = \frac{I_p - I_d}{P \cdot A}, \tag{1}$$

$$\mathrm{EQE} = R\left(\frac{hc}{q\lambda}\right), \tag{2}$$

$$D^* = R\sqrt{\frac{A}{2qI_d}}, \tag{3}$$

where I_p represents the photocurrent, I_d represents the dark current, P represents the light power density, A is the device area, h is Planck's constant, c is the speed of light, q is the electron charge, and λ represents the incident wavelength. Figures 3(e) and (f) show the R, EQE and D^* of the few-layer $MoTe_2/CdS_{0.42}Se_{0.58}$ heterojunction photodetector at a 5 V bias. From Figs. 3(e) and (f), R, EQE and D^* decreased with increasing light power density, which was mainly attributed to the trap states being fully occupied by the excited photocarriers under high power density; this resulted in a reduced density of the available states and a decreased gain [44]. This phenomenon could also be observed in other researchers' works [45]. R, EQE and D^* had maximum values of 7221 A/W, 1.52 × 10^6 % and 1.67 × 10^{15} Jones when the power density was 0.054 mW/cm^2 at a 5 V bias, respectively. These key parameters are much better than those of most reported $MoTe_2$-based photodetectors, indicating that our device possesses excellent photoelectric performance.

Periodic stability and fast response speed are important parameters of photodetectors. Figure 4 shows the *I*–*t* test diagram of the few-layer $MoTe_2/CdS_{0.42}Se_{0.58}$ heterojunction photodetector. Figure 4(a) is the *I*–*t* test of the $MoTe_2/CdS_{0.42}Se_{0.58}$ device under continuous switching cycles. Evidently, the on and off states show minimal change after 2000 s periodic illumination, indicating excellent stability and repeatability. Figure 4(b) shows the response speed diagram of the $MoTe_2$/

Table 1 Comparison of the key parameters of the CdS_xSe_{1-x} and $MoTe_2$-based photodetectors.

Device structure	Bias voltage (V)	R (A/W)	EQE (%)	D^* (Jones)	I_{light}/I_{dark}	Rise/Decay time (ms)	Ref.
$MoTe_2$ nanosheet	0	4×10^{-4}	–	1.07×10^8	–	0.043/0.043	[46]
$MoTe_2$/GeSe sheet	–5	28.4	73.5	6.0×10^9	–	0.003/0.012	[47]
$MoTe_2$/Graphene	–1	853	1.4×10^4	1.59×10^{10}	–	0.012/0.005	[48]
$CdS_{0.49}Se_{0.51}$/CdS NW	1	118	3.1×10^4	–	10^5	0.068/0.137	[49]
$MoTe_2$/Ge flake	–2	12460	–	3.3×10^{12}	–	5/5	[50]
$CdS_{0.14}Se_{0.86}$ flakes	5	703	1.94×10^5	3.41×10^{10}	–	39/39	[51]
$MoTe_2/CdS_{0.42}Se_{0.58}$ flake	5	7221	1.52×10^6	1.67×10^{15}	1.73×10^4	0.09/0.12	This work

$CdS_{0.42}Se_{0.58}$ photodetector in single on and off states under a 5 V bias. The rise time is defined as the time needed for the photocurrent to increase from 10% to 90% of the maximum value during the rising process, while the fall time is defined as the time needed for the photocurrent to decrease from 90% to 10% during the falling process in a single switch periodicity. The rise and fall times of the $MoTe_2/CdS_{0.42}Se_{0.58}$ photodetector are as short as 90/120 μs, respectively. The rapid response speed of the $MoTe_2/CdS_{0.42}Se_{0.58}$ photodetector can be attributed to the good crystal quality of the few-layer $MoTe_2$ and $CdS_{0.42}Se_{0.58}$ materials, as well as the effective interface charge separation between them. Many studies have reported millisecond or even longer response times, which limits the practical applications of photodetectors. In our study, the response time of the $MoTe_2/CdS_{0.42}Se_{0.58}$ photodetector was reduced to just 90 μs, which was significantly lower than the reported values in many photodetector fields; thus, our $MoTe_2/CdS_{0.42}Se_{0.58}$ photodetector has great application prospects.

To facilitate comparison with other reported studies, we summarized the key parameters of our $MoTe_2/CdS_{0.42}Se_{0.58}$ devices and the reported $MoTe_2$ and CdS_xSe_{1-x} based photodetectors; these are provided in Table 1. Compared with other $MoTe_2$ and CdS_xSe_{1-x} devices [46–51], the $MoTe_2/CdS_{0.42}Se_{0.58}$ devices have superior optoelectronic performance, such as high R, EQE and D^*, with a faster response speed.

Figure 5(a) shows an optical image of the few-layer $MoTe_2/CdS_{0.42}Se_{0.58}$ heterojunction device, in which the golden yellow part is the interdigital electrode. The width of the device channel is 5 μm, and the device area of the $MoTe_2/CdS_{0.48}Se_{0.58}$ device is ~1.65×10^{-7} cm^2. To determine the generation and transmission mechanism of the photocurrent in the $MoTe_2/CdS_{0.42}Se_{0.58}$ device, we first investigated the photocurrent imaging of the device corresponding to 560 nm laser excitation at a bias of 5 V, as shown in Fig. 5(b), which corresponds to the green area in Fig. 5(a). From the photocurrent imaging results, the photocurrent is mainly distributed in the overlapping region of the $MoTe_2$ and $CdS_{0.42}Se_{0.58}$ flakes, indicating that photogenerated electron-hole pairs are effectively separated at the interface. This result indicates that the heterojunction photodetector exhibits the same capability to separate photogenerated carriers as other vertical heterojunction devices. Next, we investigated the band alignment at the interface between $MoTe_2$ and $CdS_{0.42}Se_{0.58}$ based on first-principles calculations. Figure 5(c) shows the calculated projected local density of states (PLDOS) of the $MoTe_2/CdS_{0.42}Se_{0.58}$ heterojunction by using the Quantum ATK package. The calculated band gaps of $CdS_{0.42}Se_{0.58}$ and $MoTe_2$ are 2.18 eV and 0.96 eV, respectively; these are in good agreement with the experimental results. Under dark conditions, the electrons in $CdS_{0.42}Se_{0.58}$ diffuse to $MoTe_2$ driven by the band offset, while the holes in $MoTe_2$ cannot move to $CdS_{0.42}Se_{0.58}$ due to the large energy barrier at the valence band and accumulate at the interface. Due to the small band gap of $MoTe_2$ and the presence of a minority of electrons in $MoTe_2$ under dark conditions, there is a higher probability of recombination with the accumulated holes, consequently resulting in a lower dark current. Under illumination, $CdS_{0.42}Se_{0.58}$ and $MoTe_2$ absorb photons of different energies, producing a large number of photogenerated carriers. The electrons in $CdS_{0.42}Se_{0.58}$ move to $MoTe_2$, and the holes in $MoTe_2$ can also easily transfer to $CdS_{0.42}Se_{0.58}$ because the accumulation of a large number of holes in the valence band leads to a decrease in the energy barrier height. Therefore, photogenerated carriers were effectively separated [see Fig. 5(c)]. The co-absorption and efficient separation of photogenerated carriers results in a higher photocurrent and responsivity of the $CdS_{0.42}Se_{0.58}/MoTe_2$ detector. Therefore, the device exhibits a higher I_{on}/I_{off} ratio, higher responsivity, faster response speed, higher EQE and detectivity compared with the other reported $MoTe_2$-based detectors.

The imaging capability of photodetectors plays a significant role in both civilian and military fields. To explore the actual potential of the few-layer $MoTe_2/CdS_{0.42}Se_{0.58}$ photodetector, the imaging capability of the device was investigated by an imaging system [see Fig. 6(a)]. The laser passed through the U-shaped mask and illuminated the device. After the semiconductor analyzer test and imaging computer control, the U-shaped pattern on the mask plate was finally successfully reproduced, as shown in Fig. 6(b). The uniform

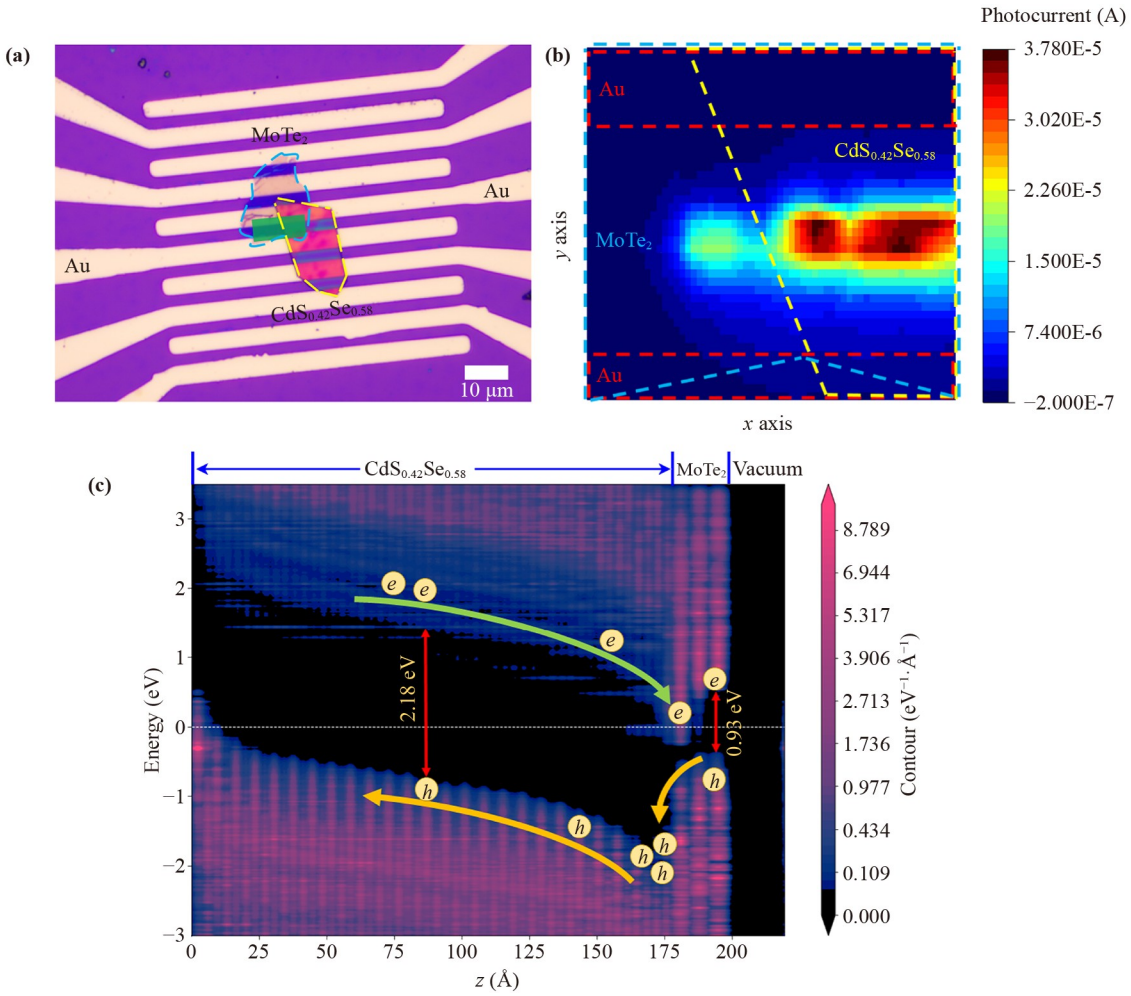

Fig. 5 **(a)** Optical microscope image and **(b)** photocurrent mapping image of $MoTe_2/CdS_{0.42}Se_{0.58}$ heterojunction device. **(c)** Calculated energy band diagram of the $MoTe_2/CdS_{0.42}Se_{0.58}$ heterojunction.

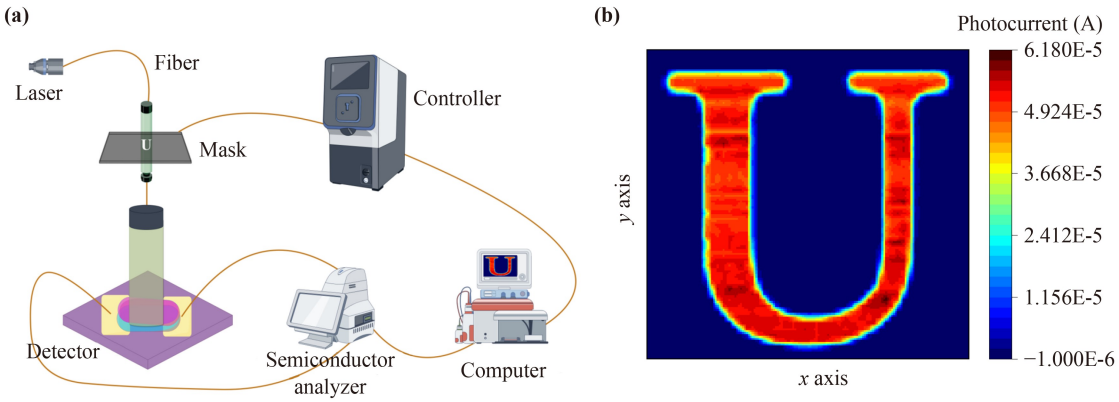

Fig. 6 **(a)** Schematic diagram of the imaging measurement system. **(b)** Imaging results of the "U" letter under visible light.

photocurrent was distributed in the U-shaped pattern, indicating that the fabricated photodetector had excellent visible light imaging capability and confirming that the few-layer $MoTe_2/CdS_{0.42}Se_{0.58}$ photodetector had unique advantages in the imaging field.

4 Conclusion

In summary, a few-layer $MoTe_2/CdS_{0.42}Se_{0.58}$ flake heterojunction photodetector was first fabricated by mechanical exfoliated and CVD methods combined with

a typical dry transfer technique. The $MoTe_2$/$CdS_{0.42}Se_{0.58}$ photodetector exhibited excellent photoelectric performance, with a higher switching ratio of 1.73×10^4, a higher responsivity of 7221 A/W, a higher EQE of 1.52×10^6 %, a larger detectivity of 1.67×10^{15} Jones and a faster response speed (rise/fall time of 90/120 μs); based on these results, our photodetector was superior to other $MoTe_2$-based photodetectors. The first-principles calculations indicated that the excellent performance of our heterojunction photodetector was attributed to the unique band arrangement at the interface. Finally, the visible light imaging function was successfully achieved on the $MoTe_2$/$CdS_{0.42}Se_{0.58}$ photodetector devices. Based on these results, our few-layer $MoTe_2$/$CdS_{0.42}Se_{0.58}$ flake photodetectors have excellent application prospects in optoelectronic devices.

Declarations The authors declare that they have no competing interests and there are no conflicts.

Acknowledgements This work was supported by the National Natural Science Foundation of China (Nos. 11864046 and 11764046), the Basic Research Program of Yunnan Province (Nos. 202001AT070064 and 202101AT070124), the Spring City Plan (High-level Talent Promotion and Training Project of Kunming) (No. 2022SCP005), and Yunnan Expert Workstation (No. 202205AF150008).

References

1. K. S. Novoselov, A. K. Geim, S. V. Morozov, D. Jiang, Y. Zhang, S. V. Dubonos, I. V. Grigorieva, and A. A. Firsov, Electric field effect in atomically thin carbon films, *Science* 306(5696), 666 (2004)
2. J. Yao, Z. Zheng, and G. Yang, All-layered 2D optoelectronics: A high-performance UV-Vis-NIR broadband SnSe photodetector with Bi_2Te_3 topological insulator electrodes, *Adv. Funct. Mater.* 27(33), 1701823 (2017)
3. A. Castellanos-Gomez, M. Poot, G. A. Steele, H. S. J. van der Zant, N. Agraït, and G. Rubio-Bollinger, Elastic properties of freely suspended MoS_2 nanosheets, *Adv. Mater.* 24(6), 772 (2012)
4. J. Yao and G. Yang, Flexible and high-performance all-2D photodetector for wearable devices, *Small* 14(21), 1704524 (2018)
5. W. Wu, L. Wang, Y. Li, F. Zhang, L. Lin, S. Niu, D. Chenet, X. Zhang, Y. Hao, T. F. Heinz, J. Hone, and Z. L. Wang, Piezoelectricity of single-atomic-layer MoS_2 for energy conversion and piezotronics, *Nature* 514(7523), 470 (2014)
6. S. Mouri, Y. Miyauchi, and K. Matsuda, Tunable photoluminescence of monolayer MoS_2 via chemical doping, *Nano Lett.* 13(12), 5944 (2013)
7. C. J. Heard, J. Čejka, M. Opanasenko, P. Nachtigall, G. Centi, and S. Perathoner, 2D oxide nanomaterials to address the energy transition and catalysis, *Adv. Mater.* 31(3), 1801712 (2019)
8. L. Tang, X. Meng, D. Deng, and X. Bao, Confinement catalysis with 2D materials for energy conversion, *Adv. Mater.* 31(50), 1901996 (2019)
9. F. R. Fan, R. Wang, H. Zhang, and W. Wu, Emerging beyond-graphene elemental 2D materials for energy and catalysis applications, *Chem. Soc. Rev.* 50(19), 10983 (2021)
10. L. X. Chen, Z. W. Chen, M. Jiang, Z. Lu, C. Gao, G. Cai, and C. V. Singh, Insights on the dual role of two-dimensional materials as catalysts and supports for energy and environmental catalysis, *J. Mater. Chem. A* 9(4), 2018 (2021)
11. P. Tao, S. Yao, F. Liu, B. Wang, F. Huang, and M. Wang, Recent advances in exfoliation techniques of layered and non-layered materials for energy conversion and storage, *J. Mater. Chem. A* 7(41), 23512 (2019)
12. Y. Tian, Y. Chen, Y. Liu, H. Li, and Z. Dai, Elemental two-dimensional materials for Li/Na-ion battery anode applications, *Chem. Rec.* 22(10), e202200123 (2022)
13. B. Li, H. Xu, Y. Ma, and S. Yang, Harnessing the unique properties of 2D materials for advanced lithium–sulfur batteries, *Nanoscale Horiz.* 4(1), 77 (2019)
14. N. Deng, Y. Feng, G. Wang, X. Wang, L. Wang, Q. Li, L. Zhang, W. Kang, B. Cheng, and Y. Liu, Rational structure designs of 2D materials and their applications toward advanced lithium–sulfur battery and lithium–selenium battery, *Chem. Eng. J.* 401(20), 125976 (2020)
15. G. Gao, F. Zheng, F. Pan, and L. W. Wang, Theoretical investigation of 2D conductive microporous coordination polymers as Li–S battery cathode with ultrahigh energy density, *Adv. Energy Mater.* 8(25), 1801823 (2018)
16. R. Rojaee and R. Shahbazian-Yassar, Two-dimensional materials to address the lithium battery challenges, *ACS Nano* 14(3), 2628 (2020)
17. A. Dodda, D. Jayachandran, A. Pannone, N. Trainor, S. P. Stepanoff, M. A. Steves, S. S. Radhakrishnan, S. Bachu, C. W. Ordonez, J. R. Shallenberger, J. M. Redwing, K. L. Knappenberger, D. E. Wolfe, and S. Das, Active pixel sensor matrix based on monolayer MoS_2 phototransistor array, *Nat. Mater.* 21(12), 1379 (2022)
18. U. Khan, Y. Luo, L. Tang, C. Teng, J. Liu, B. Liu, and H. M. Cheng, Controlled vapor–solid deposition of millimeter-size single crystal 2D Bi_2O_2Se for high-performance phototransistors, *Adv. Funct. Mater.* 29(14), 1807979 (2019)
19. S. G. Kim, S. H. Kim, J. Park, G. S. Kim, J. H. Park, K. C. Saraswat, J. Kim, and H. Y. Yu, Infrared detectable MoS_2 phototransistor and its application to artificial multilevel optic-neural synapse, *ACS Nano* 13(9), 10294 (2019)
20. S. Namgung, J. Shaver, S. H. Oh, and S. J. Koester, Multimodal photodiode and phototransistor device based on two-dimensional materials, *ACS Nano* 10(11), 10500 (2016)
21. Y. Cai, J. Yang, F. Wang, S. Li, Y. Wang, X. Zhan, F. Wang, R. Cheng, Z. Wang, and J. He, Ultrasensitive solar-blind ultraviolet detection and optoelectronic neuromorphic computing using α-In_2Se_3 phototransistors, *Front. Phys.* 18(3), 33308 (2023)

22. Z. Q. Li, T. T. Yan, and X. S. Fang, Low-dimensional wide-bandgap semiconductors for UV photodetectors, *Nat. Rev. Mater.* 8(9), 587 (2023)
23. H. Zeng, Y. Wen, L. Yin, R. Cheng, H. Wang, C. Liu, and J. He, Recent developments in CVD growth and applications of 2D transition metal dichalcogenides, *Front. Phys.* 18(5), 53603 (2023)
24. G. Zhang, Y. Shu, J. Yao, Q. Shu, H. Deng, G. Jia, and Z. Wang, Characteristics and developments of quantum-dot infrared photodetectors, *Front. Phys. China* 1(3), 334 (2006)
25. K. He, J. Zhu, Z. Li, Z. Chen, H. Zhang, C. Liu, X. Zhang, S. Wang, P. Zhao, Y. Zhou, S. Zhang, Y. Yin, X. Zheng, W. Huang, and L. Wang, High-sensitive two-dimensional PbI_2 photodetector with ultrashort channel, *Front. Phys.* 18(6), 63305 (2023)
26. C. H. An, F. Nie, R. Zhang, X. Ma, D. Wu, Y. Sun, X. Hu, D. Sun, L. Pan, and J. Liu, Two-dimensional material -enhanced flexible and self-healable photodetector for large-area photodetection, *Adv. Funct. Mater.* 31(22), 2100136 (2021)
27. R. Maiti, C. Patil, M. A. S. R. Saadi, T. Xie, J. G. Azadani, B. Uluutku, R. Amin, A. F. Briggs, M. Miscuglio, D. Van Thourhout, S. D. Solares, T. Low, R. Agarwal, S. R. Bank, and V. J. Sorger, Strain-engineered high-responsivity $MoTe_2$ photodetector for silicon photonic integrated circuits, *Nat. Photonics* 14(9), 578 (2020)
28. T. Octon, V. Nagareddy, S. Russo, M. F. Craciun, and C. D. Wright, Fast high-responsivity few-layer $MoTe_2$ photodetectors, *Adv. Opt. Mater.* 4(11), 1750 (2016)
29. L. Yin, X. Zhan, K. Xu, F. Wang, Z. Wang, Y. Huang, Q. Wang, C. Jiang, and J. He, Ultrahigh sensitive $MoTe_2$ phototransistors driven by carrier tunneling, *Appl. Phys. Lett.* 108(4), 043503 (2016)
30. H. Huang, J. Wang, W. Hu, L. Liao, P. Wang, X. Wang, F. Gong, Y. Chen, G. Wu, W. Luo, H. Shen, T. Lin, J. Sun, X. Meng, X. Chen, and J. Chu, Highly sensitive visible to infrared $MoTe_2$ photodetectors enhanced by the photogating effect, *Nanotechnology* 27(44), 445201 (2016)
31. Y. Chen, X. Wang, G. Wu, Z. Wang, H. Fang, T. Lin, S. Sun, H. Shen, W. Hu, J. Wang, J. Sun, X. Meng, and J. Chu, High-performance photovoltaic detector based on $MoTe_2/MoS_2$ van der Waals heterostructure, *Small* 14(9), 1703293 (2018)
32. M. Y. Lu, Y. T. Chang, and H. J. Chen, Efficient self-driven photodetectors featuring a mixed-dimensional van der Waals heterojunction formed from a CdS nanowire and a $MoTe_2$ flake, *Small* 14(40), 1802302 (2018)
33. J. Chen, Y. Shan, Q. Wang, J. Zhu, and R. Liu, P-type laser-doped $WSe_2/MoTe_2$ van der Waals heterostructure photodetector, *Nanotechnology* 31(29), 295201 (2020)
34. Z. Lu, Y. Xu, Y. Yu, K. Xu, J. Mao, G. Xu, Y. Ma, D. Wu, and J. Jie, Ultrahigh speed and broadband few-layer $MoTe_2$/Si 2D–3D heterojunction-based photodiodes fabricated by pulsed laser deposition, *Adv. Funct. Mater.* 30(9), 1907951 (2020)
35. R. O. Loutfy and D. S. Ng, Electrodeposited polycrystalline thin films of cadmium chalcogenides for backwall photoelectrochemical cells, *Solar Energy Mater.* 11(4), 319 (1984)
36. S. Smidstrup, D. Stradi, J. Wellendorff, P. A. Khomyakov, U. G. Vej-Hansen, M. E. Lee, T. Ghosh, E. Jónsson, H. Jónsson, and K. Stokbro, First-principles green's-function method for surface calculations: A pseudopotential localized basis set approach, *Phys. Rev. B* 96(19), 195309 (2017)
37. S. Grimme, Semiempirical GGA-type density functional constructed with a long-range dispersion correction, *J. Comput. Chem.* 27(15), 1787 (2006)
38. M. A. Hossain, J. R. Jennings, N. Mathews, and Q. Wang, Band engineered ternary solid solution CdS_xSe_{1-x} sensitized mesoscopic TiO_2 solar cells, *Phys. Chem. Chem. Phys.* 14(19), 7154 (2012)
39. S. Yang, S. Tongay, Y. Li, Q. Yue, J. B. Xia, S. S. Li, J. Li, and S. H. Wei, Layer-dependent electrical and optoelectronic responses of $ReSe_2$ nanosheet transistors, *Nanoscale* 6(13), 7226 (2014)
40. G. Chen, Z. Liu, B. Liang, G. Yu, Z. Xie, H. Huang, B. Liu, X. Wang, D. Chen, M. Q. Zhu, and G. Shen, Single-crystalline p-type Zn_3As_2 nanowires for field-effect transistors and visible-light photodetectors on rigid and flexible substrates, *Adv. Funct. Mater.* 23(21), 2681 (2013)
41. Y. H. Chen, L. X. Su, M. M. Jiang, and X. S. Fang, Switch type PANI/ZnO core-shell microwire heterojunction for UV photodetection, *J. Mater. Sci. Technol.* 105, 259 (2022)
42. S. Y. Li, Y. Zhang, W. Yang, H. Liu, and X. Fang, 2D Perovskite $Sr_2Nb_3O_{10}$ for High-Performance UV Photodetectors, *Adv. Mater.* 32(7), 1905443 (2020)
43. Y. Zhang, J. Yao, Z. Zhang, R. Zhang, L. Li, Y. Teng, Z. J. Shen, L. X. Kang, L. M. Wu, and X. S. Fang, Two-dimensional perovskite $Pb_2Nb_3O_{10}$ photodetectors, *J. Mater. Sci. Technol.* 164, 95 (2023)
44. B. X. Liu, Y. Sun, Y. Wu, K. Liu, H. Ye, F. Li, L. Zhang, Y. Jiang, and R. Wang, Enhanced photoresponse of TiO_2/MoS_2 heterostructure phototransistors by the coupling of interface charge transfer and photogating, *Nano Res.* 14(4), 982 (2021)
45. J. Yan, X. Yang, X. Liu, C. Du, F. Qin, M. Yang, Z. Zheng, and J. Li, Van der Waals heterostructures with built-in Mie resonances for polarization-sensitive photodetection, *Adv. Sci.* 10(9), 2207022 (2023)
46. J. Lai, X. Liu, J. Ma, Q. Wang, K. Zhang, X. Ren, Y. Liu, Q. Gu, X. Zhuo, W. Lu, Y. Wu, Y. Li, J. Feng, S. Zhou, J. H. Chen, and D. Sun, Anisotropic broadband photoresponse of layered type-II Weyl semimetal $MoTe_2$, *Adv. Mater.* 30(22), 1707152 (2018)
47. P. Chen, L. Pi, Z. Li, H. Wang, X. Xu, D. Li, X. Zhou, and T. Zhai, $GeSe/MoTe_2$ vdW heterostructure for UV-VIS-NIR photodetector with fast response, *Appl. Phys. Lett.* 121(2), 021103 (2022)
48. J. W. Park, Y. S. Jung, S. H. Park, H. J. Choi, and Y. S. Cho, High-performance photoresponse in ferroelectric d1T-$MoTe_2$-based vertical photodetectors, *Adv. Opt. Mater.* 10(21), 2200898 (2022)
49. P. Guo, J. Xu, K. Gong, X. Shen, Y. Lu, Y. Qiu, J. Xu, Z. Zou, C. Wang, H. Yan, Y. Luo, A. Pan, H. Zhang, J. C. Ho, and K. M. Yu, On-nanowire axial heterojunction design for high-performance photodetectors, *ACS Nano*

10(9), 8474 (2016)
50. W. Chen, R. Liang, S. Zhang, Y. Liu, W. Cheng, C. Sun, and J. Xu, Ultrahigh sensitive near-infrared photodetectors based on $MoTe_2$/germanium heterostructure, *Nano Res.* 13(1), 127 (2020)
51. J. Xia, Y. X. Zhao, L. Wang, X. Z. Li, Y. Y. Gu, H. Q. Cheng, and X. M. Meng, Van der Waals epitaxial two-dimensional CdS_xSe_{1-x} semiconductor alloys with tunable-composition and application to flexible opto-electronics, *Nanoscale* 9(36), 13786 (2017)